iScience

CellPress
OPEN ACCESS

Article

Investigating the critical characteristics of thermal runaway process for $LiFePO_4$/graphite batteries by a ceased segmented method

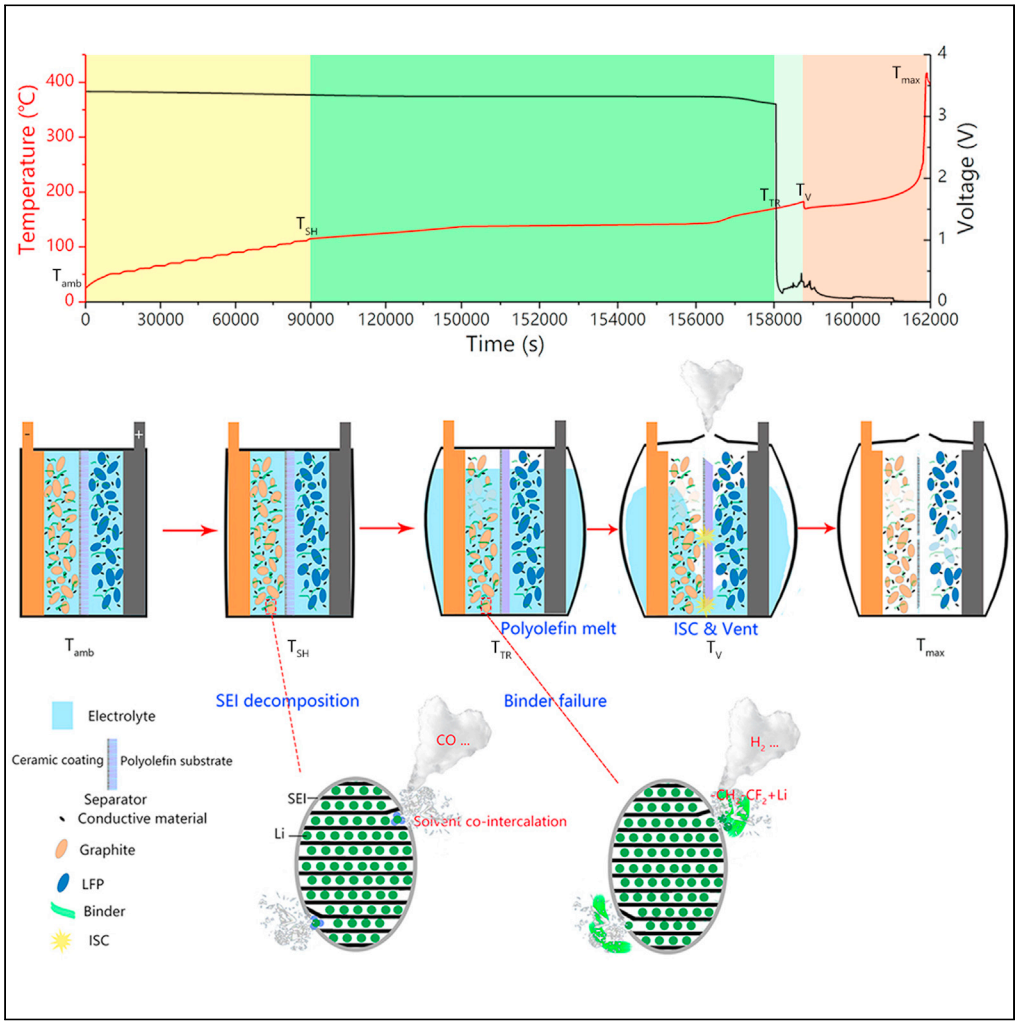

Xuan Tang, Guangxu Zhang, Xueyuan Wang, ..., Jiangong Zhu, Xuezhe Wei, Haifeng Dai

weixzh@tongji.edu.cn (X.W.)
tongjidai@tongji.edu.cn (H.D.)

Highlights

A comparative study on the thermal runaway evolution of LIBs

The gas release before venting is analyzed

The voltage shake after internal short circuit occurs is explained

The deposition/decomposition of $LiPF_6$ affects the morphology of electrodes

Tang et al., iScience 24, 103088
October 22, 2021
https://doi.org/10.1016/j.isci.2021.103088

iScience

CellPress
OPEN ACCESS

Article

Investigating the critical characteristics of thermal runaway process for $LiFePO_4$/graphite batteries by a ceased segmented method

Xuan Tang,[1,2] Guangxu Zhang,[1,2] Xueyuan Wang,[1,2] Gang Wei,[1,2] Guangshuai Han,[3,4] Jiangong Zhu,[1,5] Xuezhe Wei,[1,2,*] and Haifeng Dai[1,2,6,*]

SUMMARY

Lithium-ion batteries (LIBs) are widely used as the energy carrier in our daily life. However, the higher energy density of LIBs results in poor safety performance. Thermal runaway (TR) is the critical problem which hinders the further application of LIBs. Clarifying the mechanism of TR evolution is beneficial to safer cell design and safety management. In this paper, liquid nitrogen spray is proved to be an effective way to stop the violent reaction of LIBs during the TR process. Based on extended-volume accelerating rate calorimetry, the liquid nitrogen ceasing combined with non-atmospheric exposure analysis is used to investigate the TR evolution about $LiFePO_4$/graphite batteries at critical temperature. Specifically, the geometrical shape, voltage, and impedance change are monitored during the TR process on the cell level. The morphologies/constitution of electrodes and separators are presented on the component level. Utilizing the gas analysis, the failure mechanism of the prismatic $LiFePO_4$/graphite battery is studied comprehensively.

INTRODUCTION

Lithium-ion batteries (LIBs) have been commercialized for 30 years since 1991 (Fleming, 2015; Wang et al., 2021a, 2021b). Nowadays, LIBs are widely used as the energy storage devices for electronic products, vehicles, spacecraft, etc., owing to their relatively high power/energy density, long cycle life, no memory effect, and eco-friendly properties (Dai et al., 2021; Zhang et al., 2021; Zheng et al., 2020). However, a series of serious accidents related to LIBs indicate that the safety hazard is still a barrier for its large-scale applications in the field of transportation, especially new energy vehicles (NEVs) (Hu et al., 2020). Efforts are urgently required to investigate the thermal runaway (TR) mechanism of LIBs to develop safer NEVs.

Thermal response is directly relevant to the safety performance of LIBs. The undesirable heat with a certain chance to result in TR could be triggered by mechanical abuse (crush, penetration, vibration, etc.) (Duan et al., 2019; Wang et al., 2021a), electrical abuse (overcharge, over-discharge, short-circuit, etc.) (Ren et al., 2019a), and thermal abuse (external heating, internal heating, etc.) (Bugryniec et al., 2019). In general, the heat generated by abnormal abuse is the main precipitating factor for TR, which can destroy the original stable structure of the battery and result in a series of chain reactions including the decomposition of solid electrolyte interphase (SEI), the reaction between lithiated carbon and electrolyte, the decomposition of electrolyte, the melt of separator, the decomposition of cathode, and so on (Feng et al., 2020).

Many efforts have been made to find out the complicated mechanism of battery thermal runaway. On component level, each constituent has been tested to explore the thermal response and abuse response. For example, M. N. Richard et al. studied the thermal stability of lithium intercalated graphite in electrolytes by accelerating rate calorimetry (ARC) and found out the two reaction steps including the decomposition of metastable components of SEI and the reaction between intercalated lithium and electrolyte (Richard and Dahn, 1999). Seong-Min Bak et al. systematically investigated the thermal properties of Ni-rich ternary materials $Li(Ni_xCo_yMn_z)O_2$ ($x > 0.5$) (NCM) cathodes including NCM 433, NCM 523, NCM 622, and NCM 811 by using *in situ* time-resolved X-ray diffraction and mass spectroscopy (TR-XRD/MS) techniques (Bak et al., 2014). They analyzed the cathode phase transition in detail and found that the more Ni content is, the lower the onset temperature of the phase transition and the large amount of oxygen release are (Bak et al., 2014).

[1]Clean Energy Automotive Engineering Center, Tongji University, Shanghai 201804, China

[2]School of Automotive Studies, Tongji University, Shanghai 201804, China

[3]Institute for Advanced Study, Tongji University, Shanghai 200092, China

[4]Shanghai AI NEV Innovative Platform Co., Ltd., Shanghai 201804, China

[5]Institute for Applied Materials (IAM), Karlsruhe Institute of Technology (KIT), Eggenstein-Leopoldshafen 76344, Germany

[6]Lead contact

*Correspondence: weixzh@tongji.edu.cn (X.W.), tongjidai@tongji.edu.cn (H.D.)

https://doi.org/10.1016/j.isci.2021.103088

Joachin et al. studied the thermal stability of carbon-coated $LiFePO_4$ by differential scanning calorimeter (DSC). Their research indicates that because of the existence of strong P-O covalent bond in $(PO_4)^{3-}$, the olive $LiFePO_4$ shows better thermal stability than layered oxide cathode materials (Joachin et al., 2009).

Although there is some work concentrating on the component level, the thermal response on cell level should be conducted because the LIBs are the complex electrochemical systems which contain many kinds of active materials together to store electrical energy. Doughty et al. employed accelerating rate calorimetry (ARC) to measure the thermal response of high-power 18,650 LIBs and speculated the chemical reactions during thermal runaway process (Roth and Doughty, 2004). On that basis, Feng et al. pioneered the improved extended-volume accelerating rate calorimetry (EV-ARC) to study TR of large format LIBs and summarized three critical temperatures T_1, T_2, and T_3 which represent the onset temperature of self-heating, the TR triggering temperature, and the maximum temperature during TR process, respectively (Feng et al., 2014, 2019). To compare the thermal behaviors of LIBs built by different material systems, Lei et al. used ARC to test three kinds of 18,650 LIBs with the cathode of $LiMn_2O_4$ (LMO), $LiFePO_4$ (LFP), and $Li(Ni_{0.33}Mn_{0.33}Co_{0.33})O_2$ (NMC 111), respectively (Lei et al., 2017). They confirmed that the cell with LFP as the cathode exhibits better thermal stability, whereas the cell with NMC as the cathode shows terrible temperature tolerance (Lei et al., 2017). Moreover, the difference in maximum temperature between LFP and NMC is more than 400°C (Lei et al., 2017).

Furthermore, the toxic gaseous emission and the combustion hazards can result in serious secondary disasters for battery systems, which attract much attention from researchers. Thaler et al. studied the gas emission of 18,650 cells with three types of cathodes (LFP, NMC, and LCO/NMC) during the TR process (Golubkov and Fuchs, 2014). They found that the metal-oxide cells release huge amounts of gas rapidly, whereas the LFP cell releases a small amount of gas at a low rate (Golubkov and Fuchs, 2014). The componential analysis illustrates that the main components for metal-oxide cells are H_2, CO_2, CO, and a small amount of CH_4, C_2H_4, and C_2H_6 (Golubkov and Fuchs, 2014). In contrast, the CO emission for LFP cells only occupies a small proportion (Golubkov and Fuchs, 2014). Furtherly, Huang et al. studied the combustion behavior of 50 Ah NMC/LTO batteries (Huang et al., 2015). The combustion process was divided into three stages: igniting, stably combusting, and extinguishing (Huang et al., 2015).

However, the complex structure blocks the observation of the failure mechanism for commercial LIBs during the TR process. Understanding the change in the internal mechanism of commercial batteries during the TR process is necessary for industries. Finegan et al. applied X-ray computed tomography (CT) as a non-destructive tool to build high-spatial resolution three-dimensional (3D) images which could help researchers analyze the structural change of batteries during the TR process (Finegan et al., 2015). But this research focuses on macro-level. Disassembly is deemed to be the most effective way to study the internal change of the cell during the TR. The liquid-nitrogen-ceasing (LNC) technology is proved to be an effective way to freeze the dramatic chain reaction during the TR process. Ren et al. investigate the relationship between internal short circuit (ISC) and TR of a cell by LNC technology (Ren et al., 2021).

In this study, LNC technology combined with non-atmospheric exposure post-mortem analysis is applied to investigate the TR process by stages for the first time. A 24 Ah prismatic battery with relatively stable LFP as the cathode was chosen as the specimen. Firstly, the thermal runaway features of this battery were measured by EV-ARC. Secondly, the LNC technology was applied to stop the TR process at critical temperatures so that the post-mortem analysis could be conducted to investigate the internal mechanism of TR. The disassembly of cells is divided into five parts, including the cell at ambient temperature (T_{amb}, the subscript amb is abbreviated for ambient), self-heating temperature (T_{SH}, the subscript SH is abbreviated for self-heating), TR temperature (T_{TR}, the subscript TR is abbreviated for thermal runaway), venting temperature (T_V, the subscript V is abbreviated for venting), maximum temperature (T_{max}, the subscript max is abbreviated for maximum temperature). Besides the macroscopic and microscopic characterization, the gas emission at each node has been analyzed. Through the detailed analysis, the TR mechanism of this prismatic LFP battery is comprehensively expounded.

RESULTS

External characteristics of thermal runaway

During the thermal runaway process, LIBs suffer complex chain reactions. Figure S2 shows the temperature data and temperature rate curves during the test. Based on the test data, four critical temperatures are recognized to evaluate the thermal runaway performance of LIBs. T_{SH} is the onset temperature for detectable self-heating, which indicates the temperature of LIBs rise rate exceeds 0.02°C/min. T_{TR} is considered

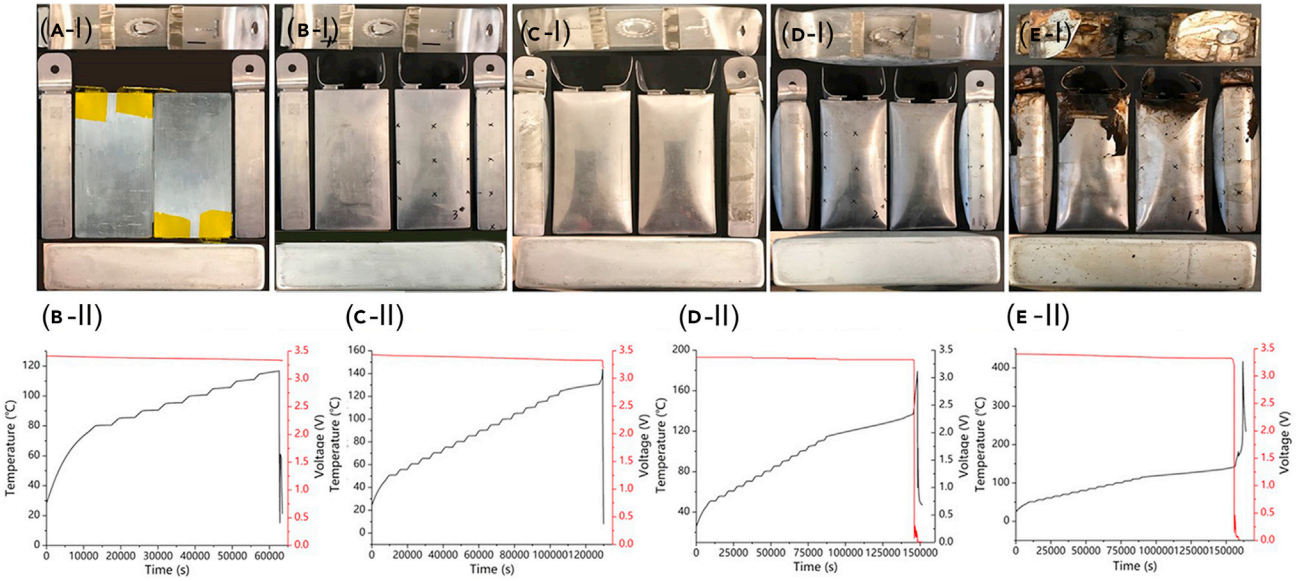

Figure 1. The comparison of LNC test results at different temperature nodes

(A-I) The geometric exterior of the cell at ambient temperature.
(B-I) The geometric exterior of the cell is heated to T_{SH}.
(B-II) Variations of voltage and temperature during the LNC test at T_{SH}.
(C-I) The geometric exterior of the swollen battery heated to T_{TR}.
(C-II) Variations of voltage and temperature during the LNC test at T_{TR}.
(D-I) The geometric exterior of the cell is heated to T_V.
(D-II) Variations of voltage and temperature during the LNC test at T_V.
(E-I) The geometric exterior of the cell is heated to T_{max}.
(E-II) Variations of voltage and temperature during the LNC test at T_{max}.

as the trigger temperature for TR, which forebodes that the exothermic reactions are so violent that the temperature rises dramatically. The definition of T_{TR} has been identified when the temperature rate of LIBs achieves 1°C/min as Figure S2 shows. T_V is the venting temperature of the cell during the TR process. T_{max} is the maximum temperature during the whole ARC test.

Then, the LNC technology is applied to freeze the cell when the cell is heated to the corresponding temperature and the results are shown in Figure 1. Figures 1A-I–E-I show the three-view photo of the cell at different temperature nodes including T_{amb}, T_{SH}, T_{TR}, T_V, and T_{max}, respectively. During the freezing process, the voltage and temperature of the cell were recorded synchronously. Figures 1B-II–E-II shows the temperature, voltage vs. time ((T-V)-t) curves when the sample was quick-frozen by liquid nitrogen at different temperature nodes including T_{SH}, T_{TR}, T_V, and T_{max}, respectively. It can be seen clearly that the sprayed liquid nitrogen freezes the cell from specific temperature to ambient temperature rapidly. It is found that the inflation of cells gets worse and worse as the temperature goes on. After venting (Figure 1D), a mass of combustion products latches onto the surface around the safety valve. The detailed information is summarized in Table 1. The voltage drops to 3.25 V at T_{TR}. Besides that, the resistance in T_{TR} increases to 40.378 mΩ, which is around 40 times larger than that of the fresh cell (0.978 mΩ). When the temperature reaches T_V, the battery expands to its maximum volume and the voltage drops to 0.329 V. In addition, the venting results in 57 g mass loss. At T_{max}, the battery loses its voltage and the mass loss is 100 g compared to the fresh one.

Thermal runaway mechanism identification

The cell cooled by liquid nitrogen spraying is disassembled in the glove box and dried out in an argon atmosphere. SEM, XPS, EDS, GC-MS tests were conducted to identify the thermal runaway mechanism.

Digital & SEM images

Figures 2, 3, and 4 show the digital photos and SEM images of anode, cathode, and separator of the specimens at different temperatures.

Table 1. The critical nodes of TR process

No.	Temperature (°C)	Weight (g)	Thickness (mm)	Voltage (V)	Resistance (mΩ)
1	T_{amb}, 25.000	551.0	30.00	3.325	0.978
2	T_{SH}, 116.743	551.0	31.22	3.319	0.986
3	T_{TR}, 170.265	550.3	41.35	3.204	40.378
4	T_V, 182.582	493.4	50.31	0.329	–
5	T_{max}, 416.788	450.9	47.08	0.005	–

With the temperature rising, the active materials show the tendency of breaking away from the current collector. For anode, the active materials have peeled off from the copper current collector partly at T_{TR} (Figure 2C-I). In comparison, cathode shows stronger stability with the intact form at the same time (Figure 3C-II). Besides that, the separator prefers to latch onto the surface of the cathode rather than anode (Figure 3C-I).

It should be noted that the electrodes become inhomogeneous as the temperature rises. For anode, beside the exposed copper current collector, two different morphologies including the gold part and black part on the surface of anode at T_V are shown in Figure 2D. The SEM images show that the graphite particles on each part are clearly visible. The difference between them is the impurity size around graphite. Figure 2E presents two different morphologies with the yellow and black part after thermal runaway (T_{max}). Figure 2E-II shows that there are a lot of small particles covering the graphite evenly in the yellow part. Figure 2E-III shows that the graphite is covered by membrane-like deposits in the black part.

For cathode, there is no obvious change occurring before T_{SH} as Figures 3A and 3B show. But the separator adheres to the cathode at T_{TR} (Figure 3C-I). By removing the separator, the cathode demonstrates three different areas as Figure 3C-II shows, which include black, grey, and abnormal parts. Comparing each SEM image with others (Figure 3C-III–3C-V)), it can be found that some neat active particles are observed in black area, film-like covering in the grey area, and agglomerated particles in the abnormal area. The melt separator attaches to the cathode tightly at T_V (Figure 3D-I). The SEM image of cathode is shown as Figure 3C-II, which shows the uniform active particles clearly. The digital photos of cathode after thermal runaway (T_{max}) show that the active materials have been peeled off from the aluminum current collector partly. Besides that, there is some wreckage of the separator remaining on the surface of the cathode (Figure 3E-I). The SEM image shows that the active materials remain homogeneous (Figure 3E-II).

The digital images of the separator are shown in Figure 4. As we can see, there is no obvious variation of separator from T_{amb} to T_{SH} (Figures 4A and 4B). But the separator melts and sticks to the cathode tightly at T_V as Figure 3D-I shows. After thermal runaway, the separator breaks into pieces as Figure 2E-I shows. The SEM images for ceramic coating show no substantial changes during the whole process, which demonstrates the excellent thermal stability of ceramic particles. In contrast, the shrinkage of polyolefin substrates is obvious. Figure 4C-IV shows that the separator has closed its micropore completely at T_{TR}. These phenomena will be analyzed in detail in the following content.

XPS spectra

Figures 5 and 6 present XPS spectra of anode and cathode respectively at different stages. C1s spectra is divided into four peaks at binding energies of 284.7 eV, 286.8 eV, 288.5 eV, and 290.1 eV, which represent the chemical bond of C-C, C-O, C=O/CO_3, and C-F, respectively (Castro et al., 2010). Three peaks are divided at binding energies of 532.0 eV and 533.4 eV for O1s spectra, which represent the chemical bond of C=O/CO_3 and C-O, respectively. F1S spectra has been divided into two peaks at 685.2 eV and 687.1 eV, which represent LiF and C-F/F-P (Castro et al., 2010). Besides that, the peaks at 133.4 eV and 136.3 eV for P2p spectra corresponding to P-O and P-F respectively (Castro et al., 2010). It is reported that the C-O and C=O/CO_3 belong to $LiCO_3$, $ROCO_2Li$, and $(CH_2OCO_2Li)_2$, which are the important components of SEI interface. C-C belongs to carbon black SP which works as the conductive agent to connect the current collector and active materials. C-F belongs to the polyvinylidene fluoride (PVDF), which works as the binder to attach active materials to the current collector; however, the P-O and P-F belong to $LiFePO_4$ and $LiPF_6$ respectively.

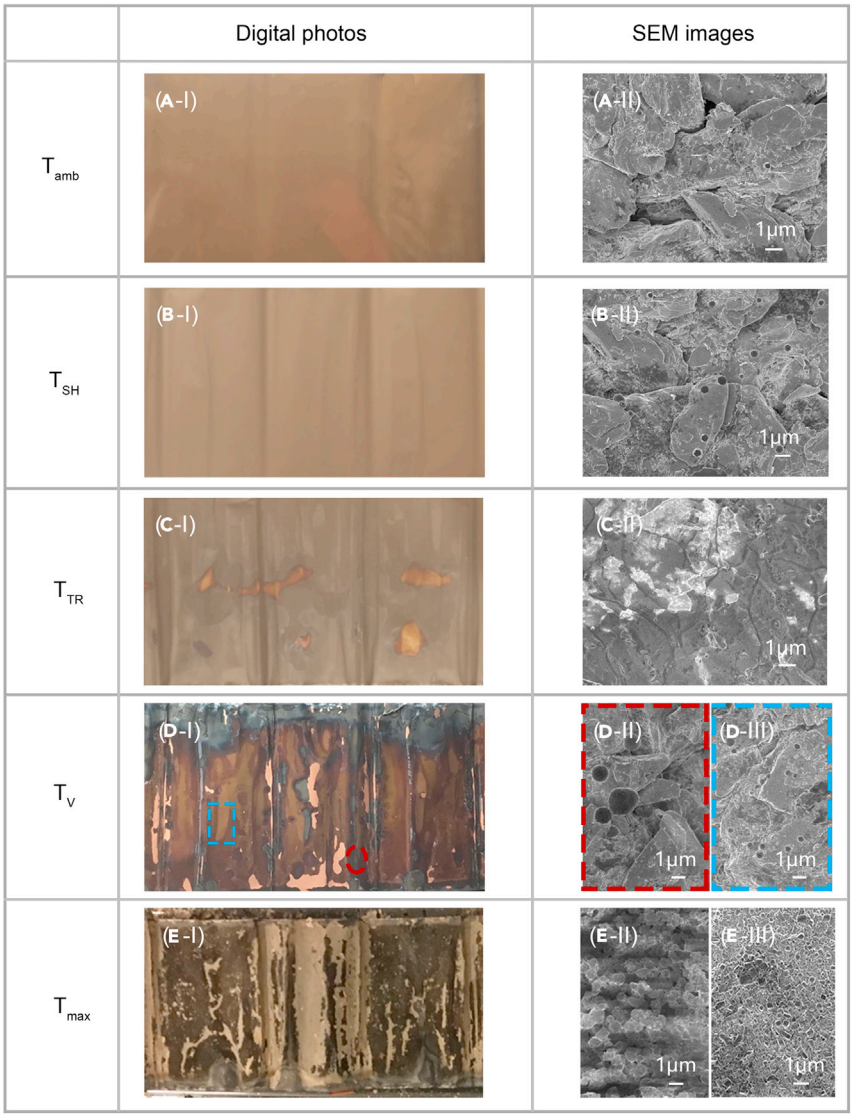

Figure 2. The anode of the dismantled battery cooled by liquid nitrogen at different temperatures

(A-I) The digital photo of the anode film dismantled from the fresh cell.

(A-II) The SEM image of the anode dismantled from the fresh cell.

(B-I) The digital photo of the anode film dismantled from the cell after being heated to T_{SH}.

(B-II) The SEM image of the anode film dismantled from the cell after being heated to T_{SH}.

(C-I) The digital photo of the anode film dismantled from the cell after being heated to T_{TR}.

(C-II) The SEM image of the anode film dismantled from the cell after being heated to T_{TR}.

(D-I) The digital photo of the anode film dismantled from the cell after being heated to T_V.

(D-II) The SEM image of the black part after heated to T_V.

(D-III) The SEM image of the gold part after heated to T_V.

(E-I) The digital photo of the anode film after heated to T_{max}.

(E-II) The SEM image of the yellow part after heated to T_{max}.

(E-III) The SEM images of the black part after heated to T_{max}.

For anode, when the temperature reaches T_{SH}, C-F, C=O, -CO_3, C-O, C-C, and LiF were detected on the surface. It can be seen that the SEI film is an important component on the surface of anode. As the temperature rises to T_V, the intensity of C-O increases significantly, which indicates the generation of metastable components (ROLi, $(CH_2OCO_2Li)_2$, and $ROCO_2Li$). After thermal runaway, the C-F, P-F, and C=O have disappeared, which indicates the decomposition of PVDF, $LiPF_6$, and metastable components of

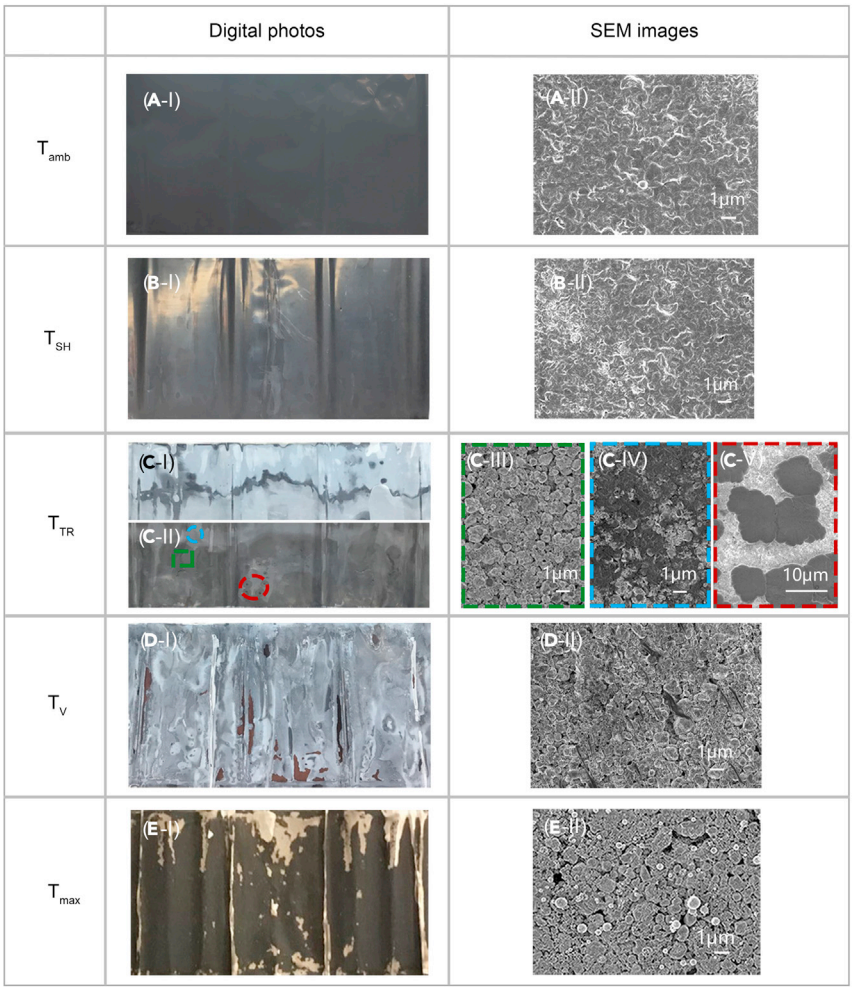

Figure 3. The cathode of the dismantled battery by LNC at different temperatures

(A-I) The digital photo of the cathode film dismantled from the fresh cell.
(A-II) The SEM image of the cathode dismantled from the fresh cell.
(B-I) The digital photo of the cathode film after being heated to T_{SH}.
(B-II) The SEM image of the black part after being heated to T_{SH}.
(C-I) The digital photo of the cathode film cuddled by the separator after being heated to T_{TR}.
(C-II) The digital photo of the cathode film by removing the separator after being heated to T_{TR}.
(C-III) The SEM image of the black part after being heated to T_{TR}.
(C-IV) The SEM image of the grey part after being heated to T_{TR}.
(C-V) The SEM image of the abnormal part after being heated to T_{TR}.
(D-I) The digital photo of the cathode film covered with molten separator after being heated to T_V.
(D-II) The SEM image of the cathode by removing the molten separator after being heated to T_V.
(E-I) The digital photo of the cathode film after being heated to T_{max}.
(E-II) The SEM image of the cathode after heated to T_{max}.

SEI interface. In contrast, the intensity of CO_3 increases significantly, indicating the final product on the negative electrode surface contains a lot of Li_2CO_3. As the intensity of C-C declines, the sp2C peak appears and increases rapidly, which belongs to the graphitized carbon. That is to say, the carbon in anode has been graphitized at T_{max}.

For cathode, C-F, C=O, -CO_3, C-O, C-C, P-O, and LiF were detected on the surface. The data for C-F, C=O, -CO_3, C-O, C-C, and LiF show similar trends like anode. As a contrast, the intensity of P-O seems to be independent of temperature, which demonstrates the excellent thermal stability of $LiFePO_4$.

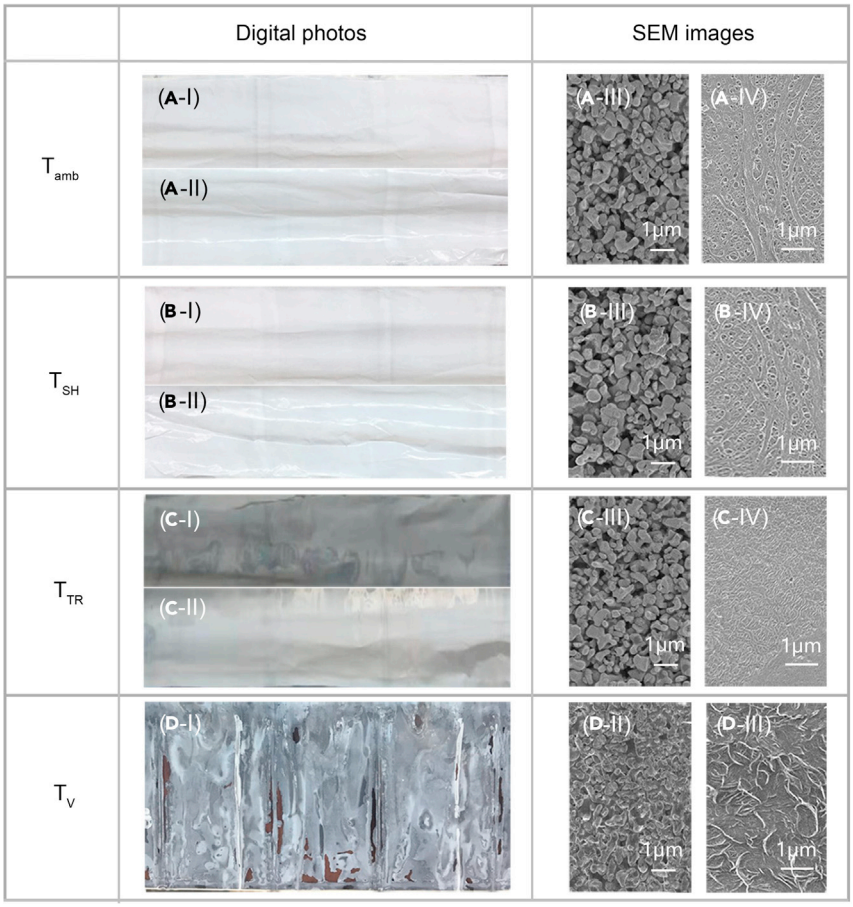

Figure 4. The separator of the dismantled battery by LNC at different temperatures

(A-I) The digital photo of the fresh separator facing cathode.
(A-II) The digital photo of the fresh separator facing anode.
(A-III) The SEM image of ceramic coating.
(A-IV) The SEM image of the PP substrate.
(B-I) The digital photo of the separator facing cathode after heated to T_{SH}.
(B-II) The digital photo of the separator facing cathode after heated to T_{SH}.
(B-III) The SEM image of the ceramic coating after heated to T_{SH}.
(B-IV) The SEM image of the PP substrate after heated to T_{SH}.
(C-I) The digital photo of the separator facing cathode after heated to T_{TR}.
(C-II) The digital photo of the separator facing cathode after heated to T_{TR}.
(C-III) The SEM image of the ceramic coating after heated to T_{TR}.
(C-IV) The SEM image of the PP substrate after heated to T_{TR}.
(D-I) The digital photo of the separator facing anode after being heated to T_V.
(D-II) The SEM image of the ceramic coating after being heated to T_V.
(D-III) The SEM image of the PP substrate after being heated to T_V.

EDS

The compositions of the deposits on electrodes are characterized by EDS, which could work as an important complement for XPS spectra. The anode cooled by liquid nitrogen shows that the content of C element decreasing as the temperature rise while the content of O, F, and P increases, which should be attributed to the complex chemical reactions including decomposition/regeneration of SEI, decomposition of $LiPF_6$ (Table 2). The cathode cooled by liquid nitrogen shows the steady content of P, which confirms the excellent thermal stability of P-O (Table 3). Besides that, Tables 2 and 5 demonstrate that there is little nitrogen element existing on the surface of anode, which proves that the rapid cooling has less effects on the cell and its post-mortem analysis.

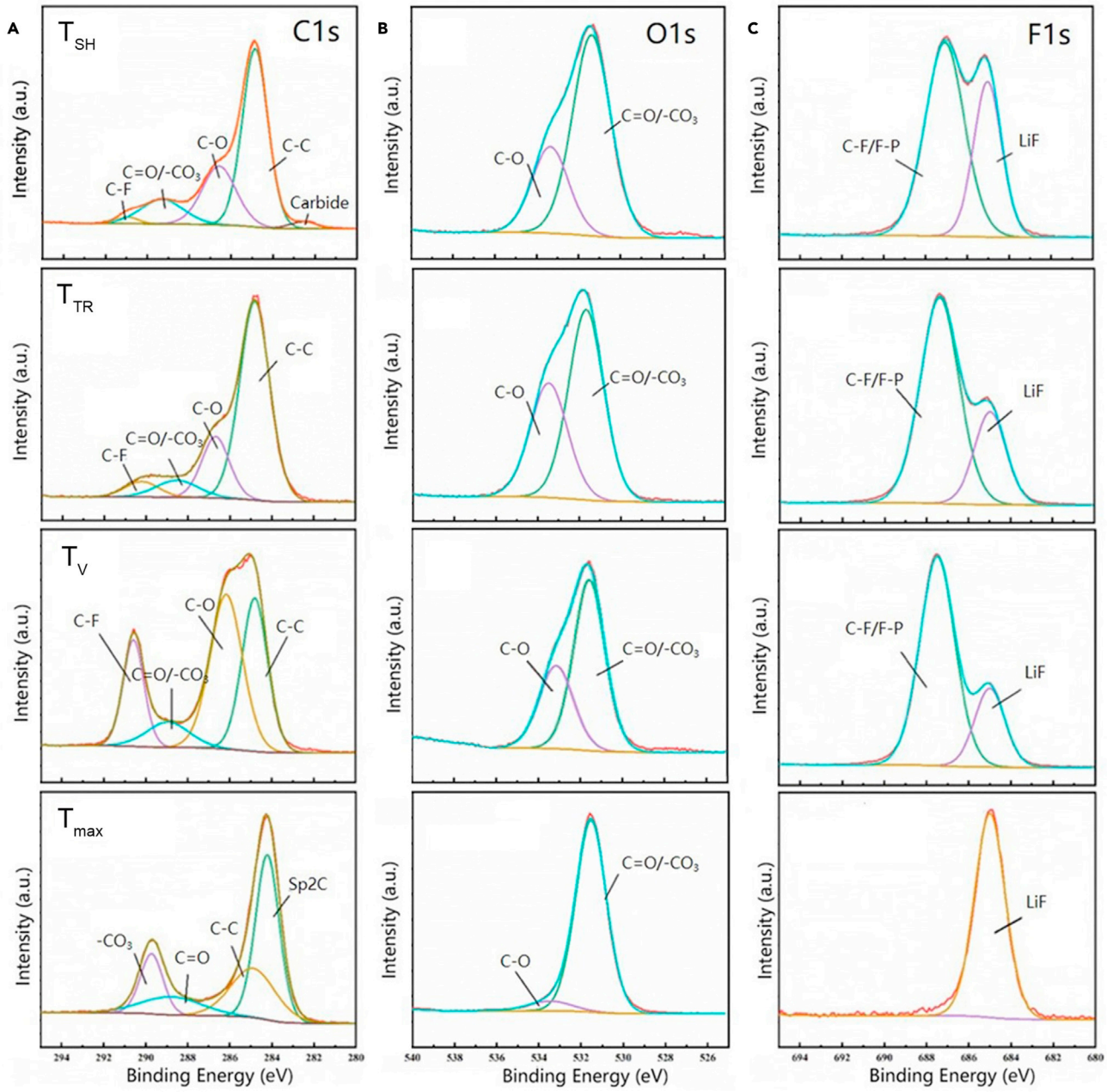

Figure 5. XPS spectra of the anode at different heated temperature

(A) C1s spectra of the anode at different temperatures.

(B) O1s spectra of the anode at different temperatures.

(C) F1s spectra of the anode at different temperatures.

It should be emphasized that the representative parts in electrodes were chosen to conduct XPS and EDS tests for electrodes.

GC-MS

The gas releasing is considered as an important cue to study the internal reactions during thermal runaway process. Figure 7 presents the gas composition analyzed by GC-MS. The analysis shows that the CO accounts for 47.07% of the gas production at T_{SH}, while the CH_4 for 31.67%, CO_2 for 12.66%, C_2H_6 for

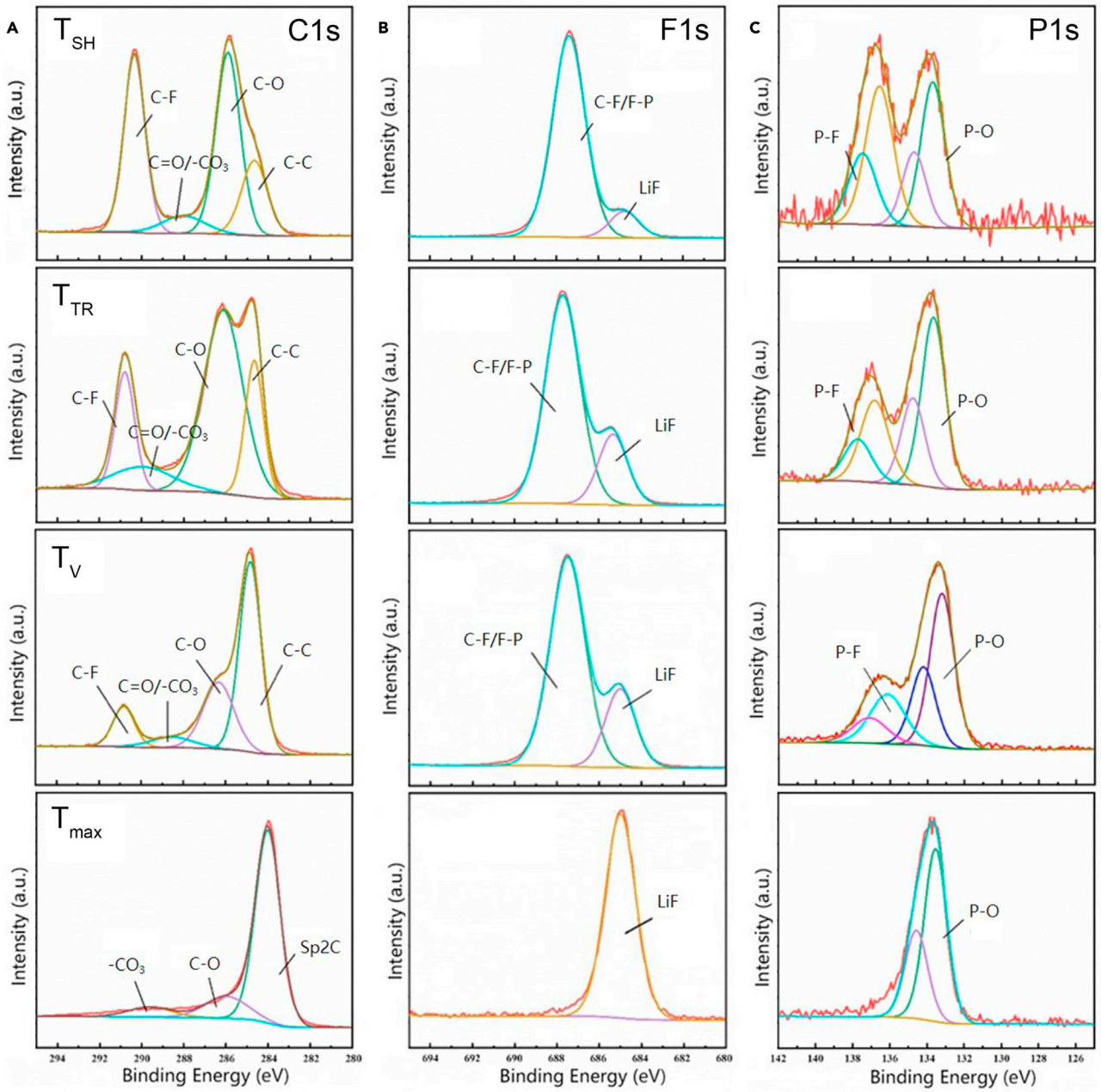

Figure 6. XPS spectra of the cathode at different heated temperatures

(A) C1s spectra of the cathode at different temperatures.

(B) F1s spectra of the cathode at different temperatures.

(C) P2p spectra of the cathode at different temperatures. Also see Figure S3.

6.08%, and so on. As a contrast, the H_2 becomes the main component at T_{TR}, which accounts for 28.08%, whereas the CO for 27.27%, C_2H_4 for 19.48%, CH_4 for 18.76%.

Self-heating (T_{SH}). The SEM images of anode and cathode taken from a liquid nitrogen cooled cell at T_{SH} are shown in Figures 2B-II and 3B-II, respectively. The graphite or LFP particles are neat-looking and are seen on the surface of electrodes. Although the morphology of electrodes at T_{SH} seems no different from the normal one at room temperature, the side reactions have resulted in the gas releasing in fact. The gas component analysis at T_{SH} is illustrated as Figure 7A shows. As we can

Table 2. EDS analysis of liquid nitrogen cooled anode at different heated temperatures

	Element content/wt. %			
Temperature (°C)	C	O	F	P
T_{SH}, 116.743	88.8	6.7	3.6	0.7
T_{TR}, 170.265	65.3	5.3	25.2	4.0
T_V,182.582	78.5	12.5	7.0	1.1
T_{max}, 416.788	24.7	13.5	59.9	1.2

see, the gases are composed of oxycarbide and hydrocarbons. The gas analysis shows that the CO is the main product for 47.07%, whereas the CH_4 for 31.67%, CO_2 for 12.66%, and C_2H_6 for 6.08%, etc. Combined with the XPS analysis, the events occurring in this stage could be summarized as follows. When the temperature rises up to the detectable temperature of self-heating (T_{SH} = 116.74°C), the metastable components (such as polymers, ROLi, $(CH_2OCO_2Li)_2$, and $ROCO_2Li$) decompose, which results in the fracture of SEI layer (Leroy et al., 2005; McArthur et al., 2012; Wang et al., 2006). The major chemical reactions are summarized as follows (Aurbach et al., 1997; Fu et al., 2015; Lai et al., 2021):

$$(CH_2OCO_2Li)_2 \rightarrow Li_2CO_3 + C_2H_4 + CO_2 + 0.5O_2 \quad \text{(Equation 1)}$$
$$2Li + (CH_2OCO_2Li)_2 \rightarrow 2Li_2CO_3 + C_2H_4 \quad \text{(Equation 2)}$$
$$2Li + 2CO_2 \rightarrow Li_2CO_3 + CO \quad \text{(Equation 3)}$$

Once the layer is broken, the active materials will lose the protection of the SEI layer and react with the electrolyte. This process is an exothermic reaction which drives the temperature up still further (Wang et al., 2012). Once the intercalated lithium is exposed to electrolyte, it would react with carbonate-based organic solvents of the electrolyte (Wang et al., 2005). The chemical reactions of this kind of batteries are summarized as follows (Lai et al., 2021; Shin et al., 2002; Spotnitz and Franklin, 2003):

$$2Li + C_3H_4O_3(EC) \rightarrow Li_2CO_3 + C_2H_4 \quad \text{(Equation 4)}$$
$$2Li + C_3H_4O_3(EC) \rightarrow 2CH_2OLi + CO \quad \text{(Equation 5)}$$
$$2Li + C_5H_{10}O_3(DEC) \rightarrow Li_2CO_3 + C_2H_4 + C_2H_6 \quad \text{(Equation 6)}$$
$$2Li + C_5H_{10}O_3(DEC) \rightarrow 2CH_3CH_2OLi + CO \quad \text{(Equation 7)}$$

In this stage, the outstanding content of CO can be regarded as the important signal to monitor the health of the battery.

Thermal runaway (T_{TR}). As time goes by, the temperature reaches thermal runaway detectable temperature (T_{TR} = 170.235°C), meanwhile, the cell swells, and the thickness increases to 41.35 mm because of the internal pressure (Figure 1B).

Anode

The disassembly photos of anode are shown in Figure 2C. The digital photo (Figure 2C-I) indicates that the active materials have been peeled off from copper current collector partly, which should be ascribed to the failure of the binder (Chen et al., 2018; Zou and Manthiram, 2020). The strong signal on H_2 (Figure 7B) is resulted from the intercalated lithium reacting with the polymer binder in the negative electrode. The reaction of metallic Li with PVDF is shown in Equation (8) (Chen et al., 2018; Jin et al., 2020; Zou and Manthiram, 2020).

Table 3. EDS analysis of liquid nitrogen cooled cathode at different heated temperatures

	Element content/wt. %				
Temperature (°C)	C	O	F	P	Fe
T_{SH}, 116.743	20.2	28.7	13.8	14.5	22.2
T_{TR}, 170.265	13.2	36.3	2.7	17.2	29.8
T_V,182.582	17.3	36.2	2.1	16.1	27.4
T_{max}, 416.788	19.3	34.3	–	16.8	27.9

Table 4. EDS analysis of liquid nitrogen cooled cathode at T_{TR}

	Element content/wt. %				
Location	C	O	F	P	Fe
Black part	13.2	36.3	2.7	17.2	29.8
Gray part	16.3	32.2	8.9	15.9	26.0
Abnormal part	7.3	7.0	65.2	15.1	5.1

$$-CH_2-CF_2+Li\rightarrow LiF+-CH=CF-+0.5H_2 \quad \text{(Equation 8)}$$

The SEM image (Figure 2C-II) shows that there are some thick membrane-like deposits on the surface of anode. The anode cooled by liquid nitrogen has been characterized by EDS in Table 2. The results present that the content of P increases sevenfold and the content of F increases sixfold, which should be ascribed to the deposition and decomposition of $LiPF_6$. The partially decomposed $LiPF_6$ will produce a large amount of LiF as Equation (9) shows.

$$LiPF_6\rightarrow LiF+PF_5 \quad \text{(Equation 9)}$$

The PF_5 produced by the decomposition of $LiPF_6$ is a strong Lewis acid which will attack the SEI layers (Yang et al., 2005). At the same time, the damaged SEI layer is repaired by the reaction between the electrolyte and intercalated Li (Kim et al., 2017). Besides that, PF_5 will react with organic solvents as Equation (10) shows, which is the reason why the amount of C_2H_4 goes up at T_{TR} (Figure 7B).

$$C_2H_5OCOOC_2H_5(DEC)+PF_5\rightarrow C_2H_5OCOOPF_4+HF+CH_2=CH_2 \quad \text{(Equation 10)}$$

Cathode

Figure 3C-I shows that the separator has adhered to the cathode tightly. Removing the separator, the intact cathode has emerged (Figure 3C-II). There are three different morphologies being found in cathode, which includes the black part marked by green dotted line in Figure 3C-III, the grey part marked by blue dotted line in Figure 3C-IV, and the abnormal part with protuberant point marked by red dotted line. The SEM image of black part is shown as Figure 3C-V. The neat-looking LFP particles are seen on the surface of the cathode (Figure 3C-III). However, some deposits on the surface of the cathode are observed in the grey part (Figure 3C-IV). In comparison, protuberant points show the agglomeration of bulky grain with the diameter of 10 μm on the surface of the cathode (Figure 3C-V). Combined with the analysis of XPS (Figure S3), we find that the different morphology of cathode is inextricably linked to the residue of $LiPF_6$ and LiF. The EDS has been applied to characterize the surface of cathode as Table 4 displays, which indicates that there is a great difference of F element for each area. The film-like material deposited on the cathode (grey part) shown in Figure 3C-IV is similar to that on anode (Figure 2C-II). The accumulation and decomposition of $LiPF_6$ (Equation 9) should be responsible for this phenomenon. For abnormal areas, the content of F reaches 65.2%, and the XPS spectra Figure S3 shows an enhanced intensity of LiF. That indicates the formation of bulky grains is attributed to the aggregation of $LiPF_6$. That is to say, the difference in morphology of cathode at T_{TR} is mainly caused by the heterogeneous deposition of $LiPF_6$.

Separator

The ceramic particles facing the anode are clearly visible, which shows excellent stability (Figure 4C-III). But the polyolefin substrate with micropores has turned into the nonporous insulating layer (Figure 4C-IV), which should be responsible for the drastic increase of impedance at T_{TR} as shown in Table 1, in which the resistance increases to 40.378 mΩ much larger than the initial value. Besides that, the melt of polyolefin substrate causes the cementation between separator and cathode (Figure 4C-I).

Table 5. EDS analysis of liquid nitrogen cooled anode at T_V

	Element content/wt. %			
Location	C	O	F	P
Black part	84.5	9.5	5.0	0.7
Gold part	78.5	12.5	7.0	1.1

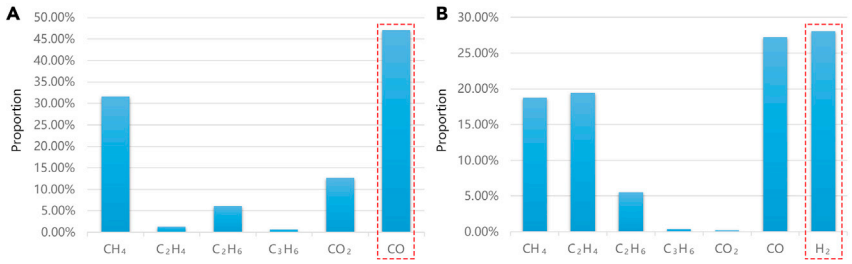

Figure 7. The gas component analysis

(A) The gas component analysis for LFP cells at T_{SH}.

(B) The gas component analysis for LFP cells at T_{TR}.

It should be emphasized that the evaporation of electrolytes can be another reason for the swelling of the battery . It is reported that the boiling points of EMC and DEC are 110°C and 126°C (Fu et al., 2016; Tang et al., 2020).

Venting (T_V). Pressure relief is an important safety function, which responds to the sudden increase of internal pressure. As the gas produced by the side reaction increases the internal pressure, the safety valve opens at T_V (182.582°C). After that, the flammable jet flow released from the safety valve is ignited, which results in violent combustion. In this stage, the cell expands to its maximum volume with a thickness of 50.31 mm.

Anode

The cell disassembly photos of anode cooled by liquid nitrogen are displayed in Figure 2D. Besides the exposed copper, the exterior appearance of anode could be divided into gold part and black part, which is closely related to the intercalated lithium. In general, the fully charged graphite anode will appear with the golden appearance (Ren et al., 2019b; Yuan et al., 2015). It is deduced that the partial exhaustion of electrolyte should be responsible for the tremendous growth of resistance and the partial discharge of electrode because the transport channel of lithium-ion is blocked. This theory explains the voltage fluctuation after the instant drop caused by massive-ISC.

The SEM images of Figures 2D-II and 2D-III demonstrate that the irregular particle morphology of graphite is clearly visible. Besides that, there are some spherical particles with a diameter around 1 μm scattered around graphite, which shows a larger size for black area rather than the gold part. The EDS was applied to characterize the surface of anode as Table 5 shows. As we can see, the content of C, O, and F in black area shows an obvious increase compared to the gold area, indicating the large generation of SEI-like substances. In a summary, the different morphologies in anode are caused by the heterogeneous reaction between active materials and electrolytes/binders.

Cathode

The cell disassembly photos of cathode are shown in Figure 3D. As we can see, the separator has attached to the cathode apparently because of the melt of PP substrates. The remains of the separator are removed to expose the cathode. The SEM image of cathode is shown as Figure 3D-II, which shows the neat-looking particles of LFP clearly. The XPS spectra (Figure 6) confirms the excellent thermal stability of P-O, which proves the LFP is stable at T_V.

Separator

The separator has melted and adhered to the cathode tightly as Figure 4D-I shows. Besides that, the melted separator absorbs some active materials from anode which is the black part of Figure 4D-I. The SEM image (Figure 4D-II) shows that the ceramic particles facing the anode are clearly visible, which shows excellent stability of ceramic coating. But the micropores of polyolefin substrate have been destroyed completely as Figure 4D-III shows.

Wreckage (T_{max}). The violent combustion has occurred. After TR, the weight loss of the cell is about 100 g compared to the initial weight of 551 g.

Table 6. EDS analysis of liquid nitrogen cooled anode at T_{max}

	Element content/wt. %				
Location	C	O	F	P	Al
Yellow part	2.6	30.5	35.5	2.6	24.4
Black part	24.7	13.5	59.9	1.2	–

Anode

The cell disassembly photo of anode is shown in Figure 2E. The digital photo of anode shows that the surface of anode can be divided into yellow and black parts. The yellow part is the remains of the separator which adhere to the surface of the electrode tightly. Figure 2E-II shows that the graphite has been covered by uniform particles with the diameter of 1 μm on the yellow area, whereas there are some thick membrane-like deposits on the surface of black part (Figure 2E-III). The EDS analysis shown in Table 6 indicates that an amount of F exists on the surface of anode, which should be the fluoride as the thin film attached to the surface of anode. The F1s spectra (Figure 5C) shows an enhanced intensity of LiF which supports this viewpoint. Besides that, the disappearance of C-O/C=O and C-C peaks indicates the complete decomposition of the SEI layer. Compared to the black area, the yellow area demonstrates the existence of the Al element which is the composition of ceramic coating for the separator (Table 6). That is to say, the Al_2O_3 coating has been separated from the fragmentized substrates and adheres to the surface of anode.

Cathode

The cell disassembly photo of cathode is shown in Figure 3E. As we can see, the active materials have been peeled off from the aluminum current collector partly, which should be ascribed to the failure of the binder. The SEM image has been taken for the active materials as Figure 3E-II shows. The LFP particles with neat appearance are clearly visible. The P2p spectra (Figure 6C) shows the excellent thermal stability of P-O too. That is to say, because of the strong P-O covalent bond in PO_4^{3-} tetrahedral structure, the LFP shows excellent thermal stability.

Based on the above analysis, the evolution of the TR process can be summarized as Figure 8 shows. As we can see, the SEI decomposition is the reason for self-heating. Besides that, the solvent co-intercalation results in the reaction between intercalated lithium and electrolytes, which produces a large amount of CO. The exposed lithium reacts with binders at higher temperature, which generates H_2 and results in the early failure of binders at anode. The high temperature also destroys the porous structure of polyolefin substrate which blocks the transport channel of Li-ions. Then, the shrinkage of the separator causes the massive-ISC of the battery and the decomposition/vaporization of electrolytes results in its inhomogeneous distribution on the surface of electrodes. Owing to the partial discharge of the electrodes caused by these two reasons, the voltage fluctuates at around 0.3V. It takes a long time for the voltage to change below 0.1V after the sudden drop occurs. At last, the combustible materials burn down, and the wreckage remains.

DISCUSSION

This paper presents a comprehensive investigation in the evolution of TR for a 24 Ah prismatic battery consisting of $LiFePO_4$/graphite under adiabatic conditions.

Four characteristic temperatures are calibrated by EV-ARC, which include the onset temperature for detectable self-heat generation (T_{SH}), trigger temperature of TR (T_{TR}), venting temperature (T_V), and the maximum temperature (T_{max}). The main innovation of this study is applying LNC technology to stop the exothermic reaction and investigate the internal mechanism of TR at each characteristic temperature with the non-atmospheric exposure post-mortem technology. In addition, the internal mechanism of TR for the battery was analyzed by the recorded external characteristic such as appearance, voltage, resistance.

The research on gas release before venting is an important contribution of this study. It is found that the decomposition of the SEI layer generates a lot of CO and the reaction between intercalated lithium and PVDF generates H_2, which can work as the early warning signals to predict TR. And the CO is generated

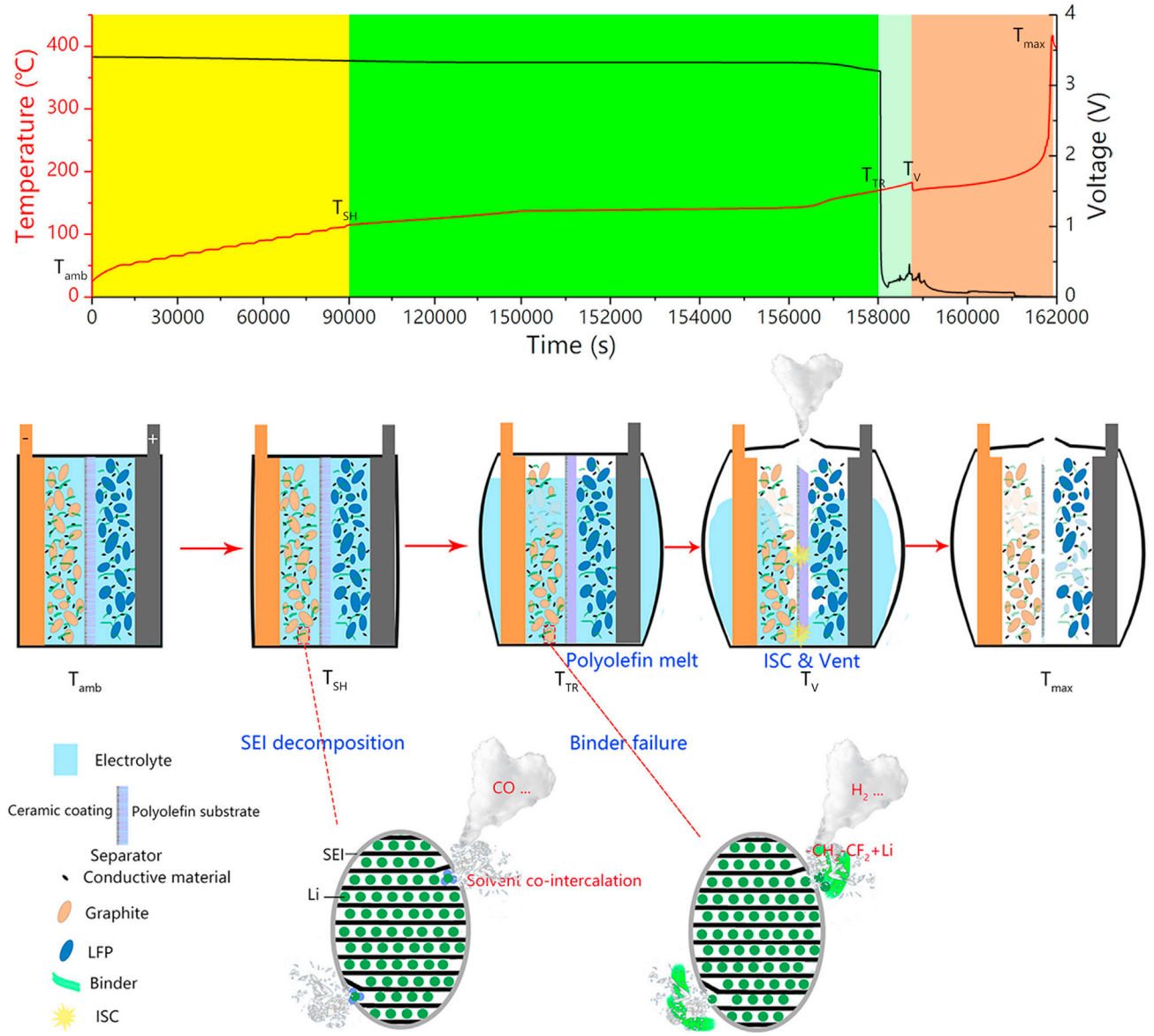

Figure 8. The schematic of TR evolution

at lower temperatures than H_2. The reaction between intercalated lithium and binders affects the appearance of anode greatly. The failure of PVDF binder results in the anode materials peeled off from the copper current collector partly at T_{TR}. As the temperature rises, the distribution of electrolytes caused by the volatilization of solvent will affect the morphology of electrodes deeply. The deposition/decomposition of $LiPF_6$ is responsible for the membrane-like deposits on the surface of electrodes during the TR process. Besides that, the lack of electrolyte can block the transport channel of lithium, which results in the tremendous growth of resistance and the partial discharge of electrodes. That's the reason for continuous voltage fluctuation after its instant drop.

Limitations of the study

Although predicting TR of LIBs by monitoring the gas release of CO and H_2 is presented in this paper, the concentration threshold needs to be confirmed. Besides that, the experiment in this study based on thermal abuse is conducted in an adiabatic environment. Therefore, more trigger conditions should be taken into consideration to explore the mechanism of TR.

STAR★METHODS

Detailed methods are provided in the online version of this paper and include the following:

- KEY RESOURCE TABLE
- CONTACT FOR REAGENT AND RESOURCE SHARING
- EXPERIMENTAL MODEL AND SUBJECT DETAILS
- METHOD DETAILS
  - Heat-wait-search (H-W-S) tests
  - Liquid-nitrogen-ceased (LNC) thermal runaway test
  - Non-atmospheric exposure post-mortem analysis

SUPPLEMENTAL INFORMATION

Supplemental information can be found online at https://doi.org/10.1016/j.isci.2021.103088.

ACKNOWLEDGMENTS

This work was financially supported by the National Natural Science Foundation of China (NSFC, Grant No. U20A20310).

AUTHOR CONTRIBUTIONS

X.T., G.H., X.W., and H.D. designed and supervised the research; G.H., and G.Z. conducted the EV-ARC test; X.W., G.W., J.Z., and X.T. conducted the characterization; G.H., and X.T. analyzed the data and prepared the figures. X.T. J.Z., and G.Z. wrote the manuscript with input from all coauthors. All the authors participated in discussions of the research.

DECLARATION OF INTERESTS

The authors declare no competing interests.

Received: April 30, 2021
Revised: August 2, 2021
Accepted: August 31, 2021
Published: October 22, 2021

REFERENCES

Aurbach, D., Zaban, A., Ein-Eli, Y., Weissman, I., Chusid, O., Markovsky, B., Levi, M., Levi, E., Schechter, A., and Granot, E. (1997). Recent studies on the correlation between surface chemistry, morphology, three-dimensional structures and performance of Li and Li-C intercalation anodes in several important electrolyte systems. J. Power Sourc. *68*, 91–98.

Bak, S.-M., Hu, E., Zhou, Y., Yu, X., Senanayake, S.D., Cho, S.-J., Kim, K.-B., Chung, K.Y., Yang, X.-Q., and Nam, K.-W. (2014). Structural changes and thermal stability of charged LiNixMnyCozO2 cathode materials studied by combined in situ time-resolved XRD and mass spectroscopy. Acs Appl. Mater. Inter. *6*, 22594–22601.

Bugryniec, P.J., Davidson, J.N., Cumming, D.J., and Brown, S.F. (2019). Pursuing safer batteries: thermal abuse of LiFePO4 cells. J. Power Sourc. *414*, 557–568.

Castro, L., Dedryvère, R., El Khalifi, M., Lippens, P.E., Bréger, J., Tessier, C., and Gonbeau, D. (2010). The spin-polarized electronic structure of LiFePO4 and FePO4 evidenced by in-lab XPS. J. Phys. Chem. C *114*, 17995–18000.

Chen, H., Ling, M., Hencz, L., Ling, H.Y., Li, G., Lin, Z., Liu, G., and Zhang, S. (2018). Exploring chemical, mechanical, and electrical functionalities of binders for advanced energy-storage devices. Chem. Rev. *118*, 8936–8982.

Dai, H., Jiang, B., Hu, X., Lin, X., Wei, X., and Pecht, M. (2021). Advanced battery management strategies for a sustainable energy future: multilayer design concepts and research trends. Renew. Sustain. Energy Rev. *138*, 110480.

Duan, J., Tang, X., Dai, H., Yang, Y., Wu, W., Wei, X., and Huang, Y. (2019). Building safe lithium-ion batteries for electric vehicles: a review. Electrochem. Energy Rev. *3*, 1–42.

Feng, X., Fang, M., He, X., Ouyang, M., Lu, L., Wang, H., and Zhang, M. (2014). Thermal runaway features of large format prismatic lithium ion battery using extended volume accelerating rate calorimetry. J. Power Sourc. *255*, 294–301.

Feng, X., Ren, D., He, X., and Ouyang, M. (2020). Mitigating thermal runaway of lithium-ion batteries. Joule *4*, 743–770.

Feng, X., Zheng, S., Ren, D., He, X., Wang, L., Liu, X., Li, M., and Ouyang, M. (2019). Key characteristics for thermal runaway of Li-ion batteries. Energy Proced. *158*, 4684–4689.

Finegan, D.P., Scheel, M., Robinson, J.B., Tjaden, B., Hunt, I., Mason, T.J., Millichamp, J., Di Michiel, M., Offer, G.J., and Hinds, G. (2015). In-operando high-speed tomography of lithium-ion batteries during thermal runaway. Nat. Commun. *6*, 6924–7024.

Fleming, W. (2015). Forty-year review of automotive electronics: a unique source of historical information on automotive electronics. IEEE Veh. Technol. Mag. *10*, 80–90.

Fu, Y., Lu, S., Li, K., Liu, C., Cheng, X., and Zhang, H. (2015). An experimental study on burning behaviors of 18650 lithium ion batteries using a cone calorimeter. J. Power Sourc. *273*, 216–222.

Fu, Y.Y., Lu, S., Shi, L., Cheng, X.D., and Zhang, H.P. (2016). Combustion characteristics of electrolyte pool fires for lithium ion batteries. J. Electrochem. Soc. *163*, A2022–A2028.

Golubkov, A.W., and Fuchs, D. (2014). Thermal runaway: causes and consequences on cell level. In Automotive Battery Technology, A. Thaler and D. Watzenig, eds. (Springer International Publishing), pp. 37–51.

Hu, X., Zheng, Y., Howey, D.A., Perez, H., Foley, A., and Pecht, M. (2020). Battery warm-up

methodologies at subzero temperatures for automotive applications: recent advances and perspectives. Prog. Energ. Combust. *77*, 100806.

Huang, P., Wang, Q., Li, K., Ping, P., and Sun, J. (2015). The combustion behavior of large scale lithium titanate battery. Sci. Rep-UK *5*.

Jin, Y., Zheng, Z., Wei, D., Jiang, X., Lu, H., Sun, L., Tao, F., Guo, D., Liu, Y., Gao, J., et al. (2020). Detection of micro-scale Li dendrite via H2 gas capture for early safety warning. Joule *4*, 1714–1729.

Joachin, H., Kaun, T.D., Zaghib, K., and Prakash, J. (2009). Electrochemical and thermal studies of carbon-coated LiFePO4 cathode. J. Electrochem. Soc. *156*, A401–A406.

Kim, J., Lee, J.G., Kim, H.-s., Lee, T.J., Park, H., Ryu, J.H., and Oh, S.M. (2017). Thermal degradation of solid electrolyte interphase (SEI) layers by phosphorus pentafluoride (PF5) attack. J. Electrochem. Soc. *164*, A2418–A2425.

Lai, X., Jin, C., Yi, W., Han, X., Feng, X., Zheng, Y., and Ouyang, M. (2021). Mechanism, modeling, detection, and prevention of the internal short circuit in lithium-ion batteries: recent advances and perspectives. Energy Storage Mater. *35*, 470–499.

Lei, B., Zhao, W., Ziebert, C., Uhlmann, N., Rohde, M., and Seifert, H. (2017). Experimental analysis of thermal runaway in 18650 cylindrical Li-ion cells using an accelerating rate calorimeter. Batteries *3*, 14.

Leroy, S., Blanchard, F., Dedryvere, R., Martinez, H., Carré, B., Lemordant, D., and Gonbeau, D. (2005). Surface film formation on a graphite electrode in Li-ion batteries: AFM and XPS study. Surf Interf. Anal *37*, 773–781.

McArthur, M., Trussler, S., and Dahn, J. (2012). In situ investigations of SEI layer growth on electrode materials for lithium-ion batteries using spectroscopic ellipsometry. J. Electrochem. Soc. *159*, A198–A207.

Ren, D., Feng, X., Liu, L., Hsu, H., Lu, L., Wang, L., He, X., and Ouyang, M. (2021). Investigating the relationship between internal short circuit and thermal runaway of lithium-ion batteries under thermal abuse condition. Energy Storage Mater. *34*, 563–573.

Ren, D., Feng, X., Lu, L., He, X., and Ouyang, M. (2019a). Overcharge behaviors and failure mechanism of lithium-ion batteries under different test conditions. Appl. Energ *250*, 323–332.

Ren, D., Hsu, H., Li, R., Feng, X., Guo, D., Han, X., Lu, L., He, X., Gao, S., Hou, J., et al. (2019b). A comparative investigation of aging effects on thermal runaway behavior of lithium-ion batteries. eTransportation *2*, 100034.

Richard, M., and Dahn, J. (1999). Accelerating rate calorimetry study on the thermal stability of lithium intercalated graphite in electrolyte. I. Experimental. J. Electrochem. Soc. *146*, 2068–2077.

Roth, E.P., and Doughty, D.H. (2004). Thermal abuse performance of high-power 18650 Li-ion cells. J. Power Sourc. *128*, 308–318.

Shin, J.-S., Han, C.-H., Jung, U.-H., Lee, S.-I., Kim, H.-J., and Kim, K. (2002). Effect of Li2CO3 additive on gas generation in lithium-ion batteries. J. Power Sourc. *109*, 47–52.

Spotnitz, R., and Franklin, J. (2003). Abuse behavior of high-power, lithium-ion cells. J. Power Sourc. *113*, 81–100.

Tang, X., Wei, X., Zhang, H., Li, D., Zhang, G., Wang, X., Zhu, J., and Dai, H. (2020). Experimental and modeling analysis of thermal runaway for LiNi0.5Mn0.3Co0.2O2/graphite pouch cell under adiabatic condition. Int. J. Energ Res. *45*, 10667–10681.

Wang, J., Mei, W., Cui, Z., Dong, D., Shen, W., Hong, J., Chen, H., Duan, Q., Wang, Q., and Sun, J. (2021a). Investigation of the thermal performance in lithium-ion cells during polyformaldehyde nail penetration. J. Therm. Anal. Calorim. *145*, 3255–3268.

Wang, X., Wei, X., Zhu, J., Dai, H., Zheng, Y., Xu, X., and Chen, Q. (2021b). A review of modeling, acquisition, and application of lithium-ion battery impedance for onboard battery management. eTransportation *7*, 100093.

Wang, Q., Ping, P., Zhao, X., Chu, G., Sun, J., and Chen, C. (2012). Thermal runaway caused fire and explosion of lithium ion battery. J. Power Sourc. *208*, 210–224.

Wang, Q., Sun, J., Yao, X., and Chen, C. (2005). Thermal stability of LiPF 6/EC+ DEC electrolyte with charged electrodes for lithium ion batteries. Thermochim. Acta *437*, 12–16.

Wang, Q., Sun, J., Yao, X., and Chen, C. (2006). Thermal behavior of lithiated graphite with electrolyte in lithium-ion batteries. J. Electrochem. Soc. *153*, A329–A333.

Yang, H., Bang, H., Amine, K., and Prakash, J. (2005). Investigations of the exothermic reactions of natural graphite anode for Li-ion batteries during thermal runaway. J. Electrochem. Soc. *152*, A73.

Yuan, Q., Zhao, F., Wang, W., Zhao, Y., Liang, Z., and Yan, D. (2015). Overcharge failure investigation of lithium-ion batteries. Electrochim Acta *178*, 682–688.

Zhang, Q., Cheng, X., Wang, C., Rao, A.M., and Lu, B. (2021). Sulfur-assisted large-scale synthesis of graphene microspheres for superior potassium-ion batteries. Energ Environ. Sci. *14*, 965–974.

Zheng, H., Hu, Z., Liu, P., Xu, W., Xie, Q., He, W., Luo, Q., Wang, L., Gu, D., Qu, B., et al. (2020). Surface Ni-rich engineering towards highly stable Li1.2Mn0.54Ni0.13Co0.13O2 cathode materials. Energy Storage Mater. *25*, 76–85.

Zou, F., and Manthiram, A. (2020). A review of the design of advanced binders for high-performance batteries. Adv. Energy Mater *10*, 2002508.

STAR★METHODS

KEY RESOURCE TABLE

REAGENT or RESOURCE	SOURCE	IDENTIFIER
Software and algorithms		
Origin 2016	OriginLab	https://www.originlab.com/index.aspx?go=PRODUCTS/Origin
Other		
EV-ARC	Thermal Hazard Technology (THT Co. Ltd.)	http://www.thermalsafetytechnology.com/product2.asp
MB 100	MBRAUN Ltd.	https://www.mbraunchina.com/cn/
SEM-EDS, JSM-7610FPLUS	JEOL Ltd.	http://www.jeol.com.cn/product/index/83
GC, Agilent Technologies 5977B MSD	Agilent Technologies	https://www.agilent.com.cn/
XPS, Thermo Scientific K-Alpha Surface Analysis	Thermal Fisher Scientific	https://www.thermofisher.cn/cn/zh/home.html?cid=ebz_bus_sbu_r04_cn_0se_bdk_bz_pur_gene_aBrand_pc_hp_051021_title

CONTACT FOR REAGENT AND RESOURCE SHARING

Further information and requests for resources and reagents should be directed to and will be fulfilled by the Lead Contact, Haifeng Dai (tongjidai@tongji.edu.cn).

EXPERIMENTAL MODEL AND SUBJECT DETAILS

The battery adopted in this investigation is a commercial prismatic lithium-ion battery with LFP as the cathode and graphite as the anode. The separator consists of polypropylene (PP) with ceramic coating. The specification of the lithium-ion cell is listed in Table S1.

METHOD DETAILS

A commercial prismatic LFP battery was selected as the experimental subject in this study. The schematic illustration of experimental steps is depicted in detail as Figure S1 shows. In summary, the core works of this experiment are summarized as the pretreatment conducted by EV-ARC & LNC and non-atmospheric exposure post-mortem analysis, specifically as follows: firstly, four critical temperatures were recognized by EV-ARC to evaluate the thermal runaway performance of battery; secondly, the specimen heated to the corresponding temperature in EV-ARC was frozen by LNC technology; thirdly, the battery was disassembled in the glove box with the argon as the shielding gas; finally, the components were transferred from glovebox to next test by the vacuum transfer box.

Heat-wait-search (H-W-S) tests

The adiabatic calorimetric environment for thermal analysis was provided by EV-ARC which was manufactured by Thermal Hazard Technology (THT Co. Ltd.). The cell was charged to 100% SOC with a current of 0.5 C before ARC experiment. The N-type thermocouple was placed on the central position of LIBs, which works as the sensor to feedback signals to EV-ARC. The experimental sequence is based on the H-W-S mode, where the heat step temperature is 5°C, followed by a wait time of 30 min. If the instrument detects the temperature-increase rate of the LIBs attaining to 0.02°C/min during the wait time, the program will identify that the test sample enters self-heating process (Figure S2). Then the program will shut down the heating and track the temperature change under an adiabatic condition.

Liquid-nitrogen-ceased (LNC) thermal runaway test

LNC TR test was conducted by liquid nitrogen spray. The EV-ARC was connected with a liquid nitrogen tank outside the chamber. During the LNC test, the temperature was monitored carefully. Once the temperature reached corresponding temperature, the liquid nitrogen would be injected into the chamber of

EV-ARC to freeze the side reactions and stop the TR process. Combining LNC test with H-W-S test, the TR process of the cell could be ceased at any time so that non-atmospheric exposure post-mortem analysis could be conducted at characteristic temperatures. In this study, the specimens have been divided into five groups, including the fresh battery at T_{amb} (No. 1), the battery heated to T_{SH} (No. 2), the battery heated to T_{TR} (No. 3), the battery heated to T_V (No. 4), and the battery heated to T_{max} (No. 5).

Non-atmospheric exposure post-mortem analysis

The frozen cell was transferred into inert gas environments (MB 100, MBRAUN Ltd.) and dismantled to collect the battery components for subsequent analysis. The vacuum transfer box was applied to transfer the samples from glovebox to next test with non-atmospheric exposure. The microstructure of the samples was characterized using a JSM-7610FPLUS Scanning Electron Microscope-Energy Dispersive Spectrometer (SEM-EDS). The samples were also analyzed by X-ray photoelectron spectroscopy (XPS, Thermo Scientific K-Alpha Surface Analysis). The compositions of the sampled gases were analyzed using a gas chromatograph (GC, Agilent Technologies 5977B MSD).